

Journal of Biomedical Optics

SPIDigitalLibrary.org/jbo

Optical diffusion performance of nanophosphor-based materials for use in medical imaging

Panagiotis F. Liaparinos

Optical diffusion performance of nanophosphor-based materials for use in medical imaging

Panagiotis F. Liaparinos

Technological Educational Institute, Department of Medical Instruments Technology, 122 10 Athens, Greece

Abstract. Recent technologies, such as nanotechnology, provide new opportunities for next generation scintillation devices and instruments. New nanophosphor-based materials seem to be promising for further improvements in optical diffusion studies. In medical imaging, detector technology has found widespread use, offering improved signal capabilities. However, in spite of many spectacular innovations and the significant research in chemical synthesis on the detective material, improvement in signal quality is still an issue requiring further progress. Here, a sophisticated analysis is shown within the framework of Mie scattering theory and Monte Carlo simulation which demonstrates the optimum structural and optical properties of nanophosphors that are significantly promising in manufacture for further signal modulation improvement. A variety of structural and optical properties were examined: (1) phosphors of grain size (1 to 1000 nm), (2) packing density (50% to 99%), (3) light wavelength (400 to 700 nm), and (4) refractive index of nanophosphor (real part: 1.4–2.0, imaginary part: 10^{-6}). Results showed that for a specific thickness of nanophosphor layer, the compromise between spatial resolution and sensitivity can be achieved by optimizing the structural (200 nm \leq grain diameter \leq 800 nm) and optical properties of the nanophosphor (1.7 \leq refractiveindex \leq 2.0). Finally, high optical modulation was accomplished employing grains of high refractive index and size above 200 nm. © 2012 Society of Photo-Optical Instrumentation Engineers (SPIE). [DOI: 10.1117/1.JBO.17.12.126013]

Keywords: optical diffusion; nanophosphors; Monte Carlo; Mie scattering; medical imaging; x-ray detectors.

Paper 12505 received Aug. 8, 2012; revised manuscript received Oct. 10, 2012; accepted for publication Oct. 26, 2012; published online Dec. 4, 2012.

1 Introduction

Medical imaging is indicated for human pathological (anatomical and physiological) investigations and its effectiveness is attributed to the differences in tissue of radiation attenuation and to the capability of the detective optical system to transform radiation to visible signals, to create an image, and finally to proceed to a specific diagnostic task.¹ The structural and optical properties of phosphor materials, used as radiation-to-light converters, affect the optical signal transferred out of the detector and play a critical role in the quality of the image and thus in diagnosis validity.

For several decades, micro powder phosphors have been employed in many commercial medical imaging modalities.² However, synthesis of nanophosphors (i.e., granular phosphor screens with grain sizes in nanoscale) has become ubiquitous over the past decade since they could replace existing phosphors for next generation, high-performance displays and devices and become a new realm of opportunity for scintillation technologies.³ On the other hand, although broad-based nanoscience research is currently being aggressively pursued and exciting new results are rapidly emerging, nanophosphors still can be thought of as a Pandora's Box, since sophisticated quantitative and qualitative understanding is lacking.⁴ In particular, the quantum confined atoms (QCA), apart from their tremendous potential for applications,^{5–7} have yielded advantages as radiation detectors that could provide possibilities on the reduction in the dosage limit in medical diagnostic examinations and also

result in images of high diagnostic quality due to the increased efficiency of light conversion and confinement.^{8–10} Nevertheless, the overall impact of nanophosphor material on signal modulation requires specialized treatment in order to determine the apparent quantum realm for high definition images and early detection of pathological features. For this reason the present study assumed the term “nanophosphor” within the size region 1 to 1000 nm (i.e., 1 to 100 nm nano-region and 100 to 1000 nm submicron-region) so as to not consider *a priori* the upper size where optimum phenomena can be made use of in medical imaging detectors.

Powder phosphor performance has been previously modeled within the framework of cascaded linear systems analysis¹¹ and historical background information in several methodologies on optical diffusion has been provided.¹² Although analytical methods based on photon diffusion equations have been preferentially employed to investigate optical diffusion, Monte Carlo simulation models can overcome cumbersome analytical modelling, inconvenience and fussiness. Monte Carlo techniques provide a significant advantage of computer science to perform experiments that would be otherwise impossible,¹³ enhance research curiosity behind scientific discovery,¹⁴ describe more accurately light propagation in anisotropic random media than anisotropic diffusion equations,¹⁵ and can ultimately enlighten the research on improved luminescence materials.¹³ Over the last 50 years, general purpose Monte Carlo radiation transport packages have been employed in medical physics¹⁶ and recently Monte Carlo models^{12,17,18} have been developed to examine optical transport of phosphor materials employed

Address all correspondence to: Panagiotis F. Liaparinos, Technological Educational Institute, Department of Medical Instruments Technology, 122 10 Athens, Greece. Tel: 00302105385387; E-mail: liapkin@teiath.gr

in commercial detective systems.¹⁹ In addition, Mie theory^{20,21} gives a complete analytical solution for the scattering of optical photons by spherical particles and provides a plausible approach to combining Monte Carlo methods with granular structures.

This paper presents the results of a comprehensive study through Mie scattering theory that aimed to: (1) analyze the physical (light wavelength, refractive index) and structural (grain size, packing density) properties of nanophosphor-based materials, (2) examine the effect of these properties on their optical parameters (the light extinction coefficient m_{ext} , the anisotropy factor g and the light absorption probability p), and (3) provide optimum optical parameters of improved optical diffusion capabilities of luminescent nanomaterials. Data obtained from this study were used to feed Monte Carlo simulation of nanophosphor layers so as to examine their signal modulation in medical imaging applications. Significant signal modulation improvement was obtained using nanograins of high refractive index with size above 100 nm (grain radius) extending the upper limit of significance²² in nanophosphor-based medical imaging instrumentation technology. The excellent features of this particular region and the level of magnitude on signal improvement tender them very promising in the manufacturing of display systems and enhance research activities in the field of medical imaging detector design and evaluation.

2 Materials and Methods

2.1 Nanophosphors: Structural and Optical Properties

Nanophosphors are a new class of advanced materials exhibiting unique structural, optical and electrical properties compared to those of their bulk materials. Advanced optical properties of nanoparticles could be achieved, owing to quantum size and surface effects originating from enlarging the band gap and widening the surface area with respect to volume of the bulk particles, respectively.³ The ability of a nanophosphor layer (as illustrated in Fig. 1) to convert the ionizing radiation to light photons affects the amount of light produced per x-ray energy deposition. Three different processes are distinguished:²³ the absorption of the ionizing radiation, the transfer of the absorbed energy to the luminescent centres and the light emission process. The lattice contains several sites, not only the intentionally added luminescent centers but also impurities defect sites, from where light photons are emitted at various light wavelengths. The activator (type and concentration) affects light efficiency as well as light wavelength. The intrinsic mechanism of photo-emission requires detailed information on the band structure as well as on the electron transference at energies above Fermi energy, and since nanomaterials exhibit different crystal structures, the concentration of activator may vary and a larger Stokes shift will reduce self-absorption. As physical size is reduced to the nanoscale regime quantum effects, surface properties and interfacial interactions become dominant and the fundamental mechanisms that usually describe the nanophosphors must be modified.²⁴

The influence of the composite mixture composition on nanophosphor structural characteristics and optical properties is investigated for the definition of some of the optimal parameters for the synthesis of powders utilisable in manufacturing radiation-to-light converters. Well-defined morphology (round

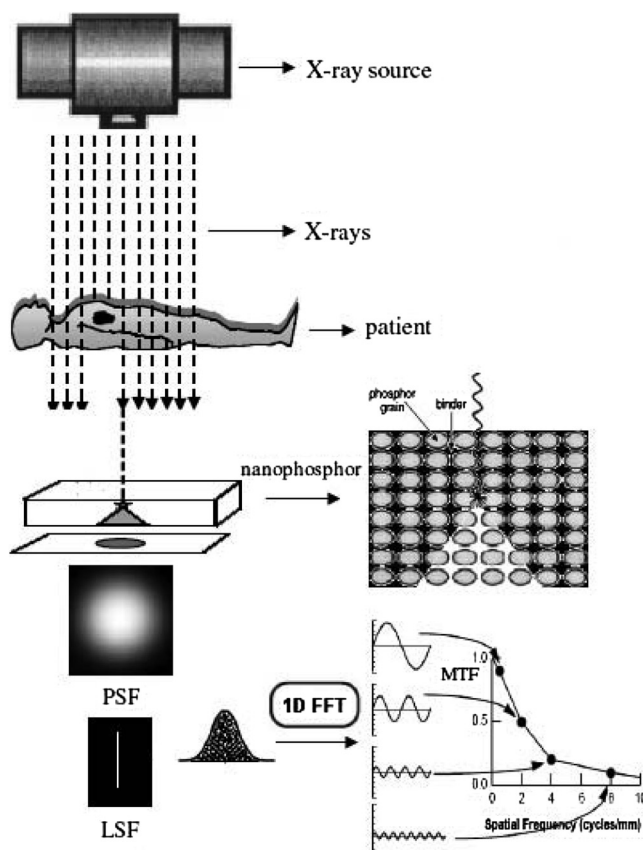


Fig. 1 A schematic illustration of x-ray medical imaging performance. Figure uses different parts of the imaging chain (some parts were taken from Refs. 25 and 26 and thereafter were suitably modified) and is used only to educate the reader. This figure depicts the evaluation of signal modulation of a nanophosphor-based indirect medical imaging system under radiation excitation. Radiation is produced from an x-ray source (e.g., an x-ray tube composed of different anode/filter combination), x-rays impinge human body, a fraction passes and is detected by the nanophosphor, x-rays are transformed to light quanta, light quanta are emitted from the surface and provide a signal which thereafter produces an image. A two-dimensional PSF is obtained by the optical photon distribution emitted by the x-ray converter which arises from the light quanta interactions with the nanograins. The line spread function (LSF) of the system is determined and, then, a fast Fourier transform (FFT) is employed so as to assess the signal transfer properties of the nanophosphor given by the MTF which shows the information carried through the modulation of the signal.

particles are preferred for their high close-packing ability) and dimension of particle can be main requirements in nanophosphor development.²⁷ In recent years, with the development of science and technology in the field of materials, a number of physical or chemical synthesis methods have been developed and successfully used for the preparation of nano-sized powders.³ The aforementioned procedures have been considered important for researchers working on nanophosphor materials where the size of the nanograin has to be restricted to 3 to 5 nm, (i.e., twice as small as that of the Bohr radii of exciton as quantum confinement regime is limited in size) and luminescence efficiency considerably increases.⁹ Although luminescence efficiency plays a crucial role in the system's sensitivity (a significant advantage in detecting the pathological features in nuclear medical imaging systems),²⁸ morphological features are accentuated by the spatial distribution of light.

The structural and optical properties of nanophosphors, regulated during the synthesis stage, play a critical role in the diffusion of light (amount and distribution). The main structural properties are the grain size as well as the packing density of the phosphor and describe the way that grains are compacted within the layer (i.e., the concentration of grains with corresponding size per unit length). The main optical properties are the light wavelength and the complex refractive index. The real part of the complex refractive index is related to light scattering and the imaginary part indicates the amount of absorption loss when the light propagates through the material. Both coefficients are dependent on light wavelength and can be coupled together properly by the frequency dependent dielectric constant using embedded Maxwell's equations where the dielectric function can then sometimes be split into bound (Lorenz) and free (Drude) contributions and interpreted in terms of the fundamental electronic band structure of the material.²⁹ A high index of refraction of phosphor nanograins causes the path of the optical photons to bend sharply, as the photons emerge from the phosphor into the adjacent void between particles. The result is that the nanophosphor is strongly scattering and light photons travel over a nearly diffusive distance in the layer. On the other hand, optical photons in a transparent layer have considerably long mean free paths.³⁰

The present manuscript provides a sophisticated research on the transmission properties of light using Mie scattering theory. The optical parameters used to describe the stochastic phenomena were based on the following structural and optical properties of the phosphor material: (1) layer composed of grains with a diameter of 1 to 1000 nm (i.e., 1 to 100 nm nano-region and 100 to 1000 nm submicron-region), (2) packing density (50% to 99%), (3) light wavelength (400 to 700 nm), which is the portion of the electromagnetic spectrum visible to the human eye, and (4) refractive index of the nanophosphor (real part: 1.4–2.0, imaginary part: 10^{-6}) where the surrounding medium was assumed to have refractive index equal to 1.35). The structural and optical parameters of nanophosphors considered in the present study are briefly given in Table 1. Evaluations were used to predict optimum optical parameters (i.e., light extinction coefficient m_{ext} , anisotropy factor g , light absorption probability p). The optical parameters were determined by employing 1.4×10^6 simulation runs of different cases as a whole.

Table 1 Structural and optical properties of nanophosphor-based materials examined in the present study: (1) Structural properties: grain size and packing density, (2) Optical properties: complex refractive index and light wavelength.

Nanomaterials—structural properties		
Packing density (%)		Grain size (nm)
50–99		1–1000
Nanomaterials—optical properties		
Refractive index		
Real part	Imaginary part	Light wavelength (nm)
1.4–2.0	10^{-6}	400–700

2.2 Light Interactions with Nanograins: Optical Parameters

After light generation, light quanta are emitted following isotropic distribution. Within the material structure, nanograin can be thought of as a partially light absorbing center also changing the orientation of transmitted light. Light attenuation is directly affected by the structural and optical properties of nanograins and could be provided by the following procedures (see Appendix A): (1) light extinction until interaction which is described by the light extinction coefficient m_{ext} , (2) decision of either light scattering or light absorption in the site of interaction which is described by the probability of light absorption p and (3) determination of the new direction of the scattered light photon (in case of light scattering) which is described by the anisotropy factor g .

The effect of m_{ext} on the first stage (i.e., light extinction) can be shown in Fig. 2(a) where high values of m_{ext} increase light interactions with nanograins and cause light photons to follow shorter trajectories until reaching the output of the nanophosphor layer surfaces. When light suffers higher attenuation, lateral light spread is reduced and sharper point spread function (PSF) is obtained on the layer output side improving the signal transfer properties of the nanophosphor (Fig. 1). Light absorption is also affected by the probability p at each site of light interaction (second stage) where either light absorption or light scattering take place in nanograins, as shown in Fig. 2[b(i)] and 2[b(ii)], respectively. The effect of g on the third stage (i.e., light scattering) can be shown in Fig. 2(c) where high values of g correspond to light scattering at small angles and therefore maintain their initial direction. As light production process follows an isotropic distribution, if light photons maintain their initial direction (i.e., $g = 1$, sharply forward direction), the PSF of light emitted quanta keeps its initial spread. In the other case, (i.e., $g < 1$) light distribution is characterized by a more sharply forward direction of light quanta. This may provide an advantage of nanophosphor with low anisotropy factor values where light diffusion is limited to lower solid angles within this layer and implies a more sharp angular distribution of light spread toward layer output surface.³¹

Although all optical parameters affect light transmission and optical signal modulation changes according to their values, significant improvement is accomplished mainly through light absorption (i.e., m_{ext} and p) which reduces lateral spread. For example, traditional or recent techniques for resolution improvement, such as grains incorporated with absorbing dyes or sintering methods,³² are based on changing either the optical properties of nanophosphors (i.e., the refractive index) and therefore the absorption of each light photon in case of interaction (i.e., p) or the structural properties of nanophosphors (i.e., the packing density), thus the key parameter for nanophosphors of different grain porosity is the m_{ext} .

2.3 Geometry of the Monte Carlo Simulation Model

A nanophosphor-based material, composed of phosphor nanograins, was modeled as a three-dimensional layer. The converter was considered a cascade linear system of discrete stages. A cascaded linear systems model has been shown to accurately describe the signal of imaging systems considering that the system has a linear and shift-invariant signal response. Furthermore, the system was assumed ergodic and stationary, so that

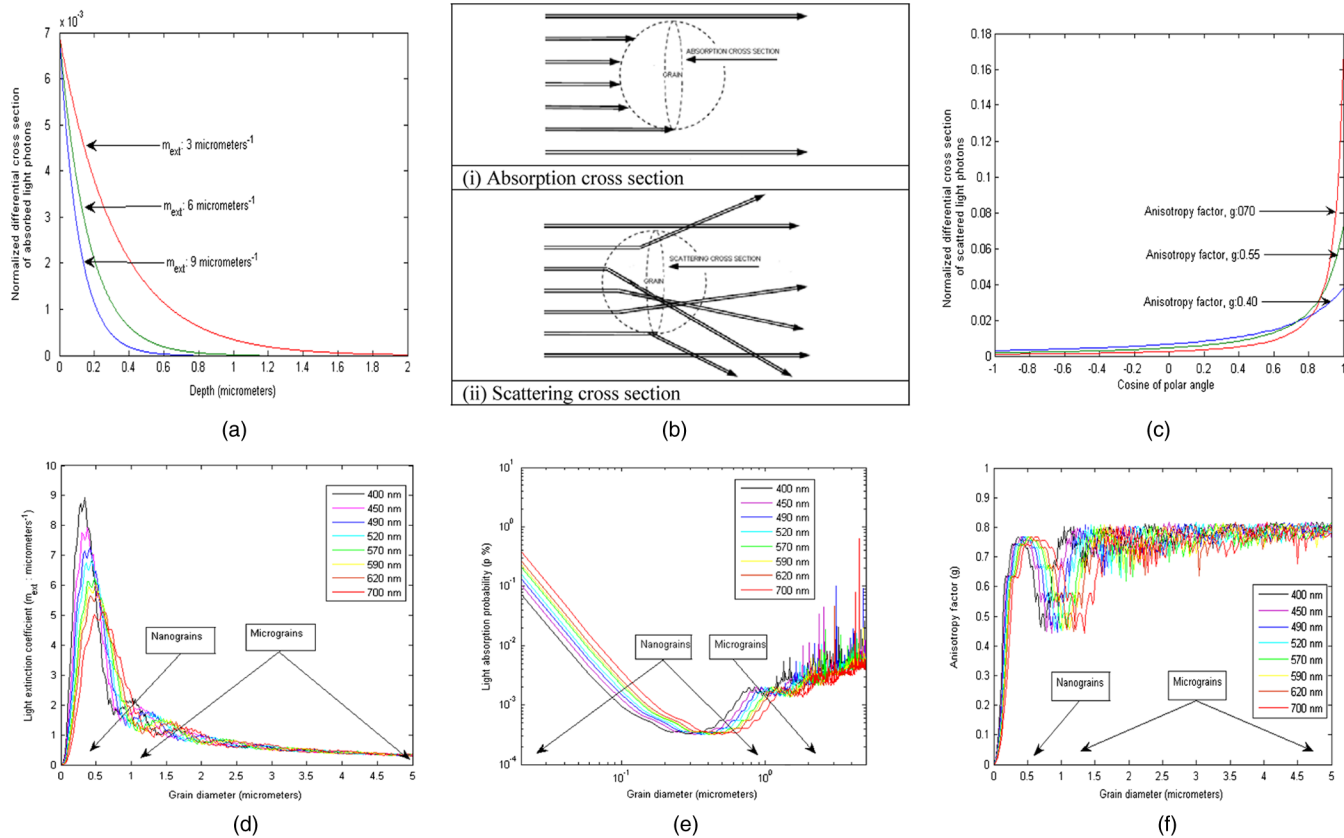


Fig. 2 Figure illustrates the intrinsic mechanisms of light diffusion within the nanophosphor: light extinction until interaction which is described by the light extinction coefficient m_{ext} , decision of either light scattering or light absorption in the site of interaction which is described by the probability of light absorption p and determination of the new direction of the scattered light photon (in case of light scattering) which is described by the anisotropy factor g . Figure includes: (a) The variation of free path length (fpl) of the light photons as a function of layer depth (from the site of interaction) for various values of light extinction coefficient m_{ext} (3, 6, 9 μm^{-1}), (b) Light interaction with phosphor grain: (i) Light absorption and (ii) Light scattering, (c) The variation of the normalized number of scattered light photons as a function of the scattered polar angle (cosine) for various values of anisotropy factor g (0.4, 0.55, 0.7), (d) The variation of light extinction factor m_{ext} as a function of grain diameter (0.01–5 μm) and (e) The variation of light absorption probability p as a function of grain size (logarithmic scale) as a function of grain diameter (0.01–5 μm) and (f) The variation of anisotropy factor g as a function of grain radius (0.01–5 μm). Optical parameters were predicted assuming packing density 50%, refractive index (real part: 2.0, imaginary part: 10^{-6}) and light wavelength in the visible region: violet: (400–450 nm), blue: (450–490 nm), cyan: (490–520 nm), green (520–570 nm), yellow (570–590 nm), orange (590–620 nm), red (620–700 nm).

the individual pixel noise may be determined from a single pixel measured repeatedly. The cascaded systems approach represents the imaging system as a series of discrete stages, where each stage represents either a quantum gain or spatial spreading (blurring) process.¹¹ In x-ray medical imaging, radiation impinges the layer and thereafter interacts with the converting material producing optical photons. The emitted optical photons are partially attenuated within the converter through light interactions with the nanograins (see Appendix B) and thereafter exit the surface of the layer contributing to the measured signal. In this study, radiation impinges on the nanophosphor following depth of interaction equal to the half of nanophosphor thickness for each case. The reasons to proceed to this selection certain to the following considerations: (a) It is not necessary to provide physical properties (e.g., chemical composition and density) of the nanophosphor, which affect the radiation attenuation properties of the material from which fluctuations on the final signal are observed.³³ This consideration is very important for the present study so as to focus only on the optical diffusion capabilities of the nanomaterial. For similar purposes, the x-ray scattering effects on light characteristics were excluded as well fluorescence x-rays and Auger electrons. X-ray photons followed only photoelectric absorption and the x-ray energy

was absorbed locally in the interaction site, (b) Light emission and transmission follows a symmetry distribution on both sides of the layer output independently of the depth of the x-ray interaction,³⁴ thus the effect on optical blurring and light modulation is due only to the structural and optical properties of the nanophosphor. The PSF of light quanta of each case of nanophosphor is obtained from an average encountered number of light quanta taken from 10 simulation runs. 10^5 light photons were produced for each simulation. As long as this amount of light is large, the present Monte Carlo calculations describe the optical performance of nanophosphors adequately, independent of optical quantum noise effects on light characteristics due to their interaction with phosphor nanograins. Light quanta were encountered on the surface of the layer (with common thickness value 200 μm) divided in a matrix of pixels (pixel size: 78.125 μm). However, the optical performance of the nanomaterial was independent from the effect of pixel size [see Eq. (27) in Appendix C].

2.4 Signal Modulation Performance

The signal modulation typically contains information transmitted from the nanophosphor layer, under radiation excitation,

during the blurring processes of the spatial distributed light quanta¹¹ (i.e., stochastic processes of light interactions with the nanograins). Of greater utility is the shape of the response of the system to a delta function. This response is called the PSF. It contains all of the deterministic spatial-transfer information of the system. The signal transfer properties describe the capability of the nanophosphor layer to distinguish several shapes of objects.¹ That is, adjacent pixels evince shades of gray in response to patterns of varying spatial frequency, and hence the actual capability to show fine detail, whether with full or reduced contrast. The improved signal modulation of some materials can enhance the validity of diagnosis and thereafter lead to the early detection of pathological features within an organ as well as to the early detection of tumors. Signal modulation can be evaluated by the modulation transfer function (MTF), which is the equivalent of frequency response of the nanophosphor layer. The spatial distribution of light quanta varies mainly due the stochastic processes of optical diffusion. The signal transfer characteristics of a phosphor-based x-ray converter can be expressed by the MTF (see Appendix C).

3 Results and Discussion

The variation of the optical parameters (i.e., the light extinction coefficient m_{ext} , the light absorption probability p and the anisotropy factor g) as a function of grain size is illustrated in Fig. 2(d)–2(f) for various cases. According to the variability of optical parameters, we can define three regions as a function of grain size: (1) region of nanograins, (2) region of limiting micrograins, and (3) region of micrograins. It is very important to note that improved optical parameters can be obtained in all regions according to the structural and optical properties of the material. A key parameter for shifting the optimum parameters on nanoscale is the refractive index of the phosphor. In addition, although an increase in the refractive index causes a shift in lower grain sizes, the optical parameters change considerably in magnitude.

For example, optimum optical parameters are obtained in: (a) nanoscale for high values of refractive index (e.g., 2.0) and (b) micro-scale for low values of refractive index (e.g., 1.4). However, as refractive index increases from 1.4 to 2.0, optical parameters change their values considerably (e.g., m_{ext} changes approximately from $0.23 \mu\text{m}^{-1}$ up to $8.9 \mu\text{m}^{-1}$). Furthermore, optimum parameters for a specific light wavelength (e.g., 400 nm) are restricted within a small range of grain size distribution (200 to 500 nm) for high refractive index (2.0). This range could be considered nanophosphor grains of higher diameter (300 to 700 nm) by reducing the refractive index. Regarding light wavelength, shifts to higher wavelengths (from violet to red) increase the capability to develop nanophosphors composed of larger phosphor nanograins (800 to 1000 nm). According to the aforementioned considerations, Table 2 summarizes the optimum Mie optical parameters based on the structural and optical properties of nanophosphors described in Table 1. We should note that strain effects³⁵ on the reduction of the complex refractive index (see Appendix D) have been taken into account for quantum dots (size in the range 3 to 5 nm). Four main categories were encountered for further examination through Monte Carlo modeling: (1) nanophosphor (case 1) composed of nanograins sized in the range of 3 to 5 nm (quantum dots): m_{ext} ($0.00205 \mu\text{m}^{-1}$), g (0.00215), $p\%$ (96.61), (2) nanophosphor (case 2) composed of nanograins sized in the range 800 to 1000 nm (refractive

index around 1.4), m_{ext} ($0.1 \mu\text{m}^{-1}$), g (0.94), $p\%$ (0.012), (3) nanophosphor (case 3) composed of nanograins sized 600 to 800 nm (refractive index around 1.7), m_{ext} ($3 \mu\text{m}^{-1}$), g (0.88), $p\%$ (6×10^{-4}), (4) nanophosphor (case 4) composed of nanograins sized 200 to 600 nm (refractive index around 2.0), m_{ext} ($6 \mu\text{m}^{-1}$), g (0.70), $p\%$ (4.5×10^{-4}).

Figure 3(a)–3(d) shows the ground sides of PSF for the aforementioned categories. It was found that optical diffusion is significantly improved using nanophosphor materials with high light attenuation properties (mainly obtained by high values of m_{ext}), shifting the grain diameter from 1000 nm down to 200 nm and by increasing the refractive index of the nanophosphor. Figure 3(e) depicts the MTF curves of all cases considered (cases 1–4). As derived and shown in Fig. 3(e), comparing the signal modulation of nanophosphors above 200 nm (i.e., cases 2, 3, and 4) with that of nanophosphor (case 1) where optical properties have been considered more attractive due to strain effects and high luminescence efficiency, the percentage signal modulation was found significantly improved. Signal modulation improvement was found to increase rapidly at low frequencies, reaching a maximum and thereafter presents a slight drop at higher frequencies. In particular, signal modulation improvement was maximized approximately by 125.42% at 17 cycles/cm (case 2), 252.98% at 19 cycles/cm (case 3), and 327.44% at 26 cycles/cm (case 4). Signal modulation was predicted in all spatial frequencies with maximum relative standard deviation (RSD): 0.74% for case 2, 0.82% for case 3 and 1.20% for case 4.

As signal modulation improvement occurs at lower grains sizes by increasing the refractive index of the material, researchers could consider a further increase of the refractive index so as to predict higher light attenuation probabilities even in the range 3 to 5 nm. However, this fact could lead to lower amount of light emitted. The present investigation also found that nanophosphor (case 3) exhibited approximately 44.90% (RSD: 0.44%) of the produced light while nanophosphor (case 4) approximately 25.85% (RSD: 2.53%). Thus, for a specific thickness of nanophosphor layer the compromise between spatial resolution and sensitivity can be achieved by optimizing the structural ($200 \text{ nm} \leq \text{grain diameter} \leq 800 \text{ nm}$) and optical properties of the nanophosphor ($1.7 \leq \text{refractive index} \leq 2.0$). A point worth commenting is that quantum dots (case 1) showed considerably high light self-absorption due to the high value of p (96.61% for 3 nm nanoparticle) emitting approximately 30.28% (RSD: 2.25%) of the light produced. Taking also into account their degrading spatial distribution of light, this may provide a disadvantage for their use in the synthesis of nanophosphor-based x-ray detective materials.³⁶

Finally, it would be of significance to note that the findings of the present study could be extended to uses in other instrumentations which incorporate material structures composed of nanograins with demands of high spatial resolution imaging, such as: detecting tools of biological structures,³⁷ storage phosphor imaging,³⁸ and phosphor-based white light emitting diode applications³⁹ and optical probes taking into account issues relative to sensor manufacturing.⁴⁰ The performance of the optical modeling and optimization could enhance research on particle characterization methods, microscopy techniques⁴¹ homeland security as well as national defense applications⁴² and finally could have an impact on other scientific fields including chemical, energy, optoelectronic and space industries.⁴³

Table 2 Optimum optical parameters of nanophosphor-based materials of several structural and optical properties.

	Nanograins									
	$n = 1.4$			$n = 1.7$			$n = 2.0$			
	$n_{\text{ext}} (\mu\text{m}^{-1})$	g	$p(\%)$	$m_{\text{ext}} (\mu\text{m}^{-1})$	g	$p(\%)$	$n_{\text{ext}} (\mu\text{m}^{-1})$	g	$p(\%)$	$p(\%)$
Violet	0.18-0.23	0.95-0.97	7×10^{-3} - 10×10^{-3}	3.2-4.4	0.83-0.90	5×10^{-4} - 7×10^{-4}	5.3-8.9	0.63-0.77	3×10^{-4} - 6×10^{-4}	
$\lambda(\text{nm})$ 400-450		$r(\text{nm})$ 400-500			$r(\text{nm})$ 200-400			$r(\text{nm})$ 100-250		
Blue	0.12-0.18	0.95-0.97	8×10^{-3} - 11×10^{-3}	3.2-3.9	0.86-0.90	5×10^{-4} - 6×10^{-4}	4.1-7.9	0.61-0.77	3×10^{-4} - 6×10^{-4}	
$\lambda(\text{nm})$ 450-490		$r(\text{nm})$ 400-500			$r(\text{nm})$ 250-400			$r(\text{nm})$ 100-275		
Cyan	0.11-0.15	0.94-0.96	9×10^{-3} - 12×10^{-3}	3.2-3.6	0.88-0.90	5×10^{-4} - 6×10^{-4}	4.9-7.3	0.63-0.77	3×10^{-4} - 6×10^{-4}	
$\lambda(\text{nm})$ 490-520		$r(\text{nm})$ 400-500			$r(\text{nm})$ 300-400			$r(\text{nm})$ 125-300		
Green	0.09-0.13	0.93-0.96	10×10^{-3} - 13×10^{-3}	2.8-3.3	0.86-0.90	5×10^{-4} - 7×10^{-4}	3.7-6.9	0.63-0.77	3×10^{-4} - 7×10^{-4}	
$\lambda(\text{nm})$ 520-570		$r(\text{nm})$ 400-500			$r(\text{nm})$ 300-500			$r(\text{nm})$ 125-350		
Yellow	0.08-0.11	0.93-0.95	11×10^{-3} - 14×10^{-3}	2.7-3.1	0.86-0.90	5×10^{-4} - 6×10^{-4}	3.3-6.2	0.61-0.77	3×10^{-4} - 6×10^{-4}	
$\lambda(\text{nm})$ 570-590		$r(\text{nm})$ 400-500			$r(\text{nm})$ 300-500			$r(\text{nm})$ 125-350		
Orange	0.07-0.10	0.92-0.95	11×10^{-3} - 15×10^{-3}	2.7-3.0	0.87-0.90	5×10^{-4} - 6×10^{-4}	4.2-6.0	0.63-0.77	3×10^{-4} - 6×10^{-4}	
$\lambda(\text{nm})$ 590-620		$r(\text{nm})$ 400-500			$r(\text{nm})$ 350-500			$r(\text{nm})$ 150-350		
Red	0.06-0.09	0.90-0.94	12×10^{-3} - 17×10^{-3}	2.2-2.8	0.85-0.89	5×10^{-4} - 6×10^{-4}	3.6-5.8	0.67-0.77	3×10^{-4} - 6×10^{-4}	
$\lambda(\text{nm})$ 620-700		$r(\text{nm})$ 400-500			$r(\text{nm})$ 350-500			$r(\text{nm})$ 200-400		
Nanograins (quantum confinement)										
$n: 1.4-2.0$	$9.18 \times 10^{-6} < m_{\text{ext}} (\mu\text{m}^{-1}) < 2.05 \times 10^{-3}$			$2.15 \times 10^{-4} < g < 2.2 \times 10^{-3}$			$0.58 < p(\%) < 96.61$			
$\lambda(\text{nm})$ 400-700	Nanograins with absorbing dyes			High packed nanograins						
	$m_{\text{ext}} (\mu\text{m}^{-1})$	g	$p(\%)$	$m_{\text{ext}} (\mu\text{m}^{-1})$	g	$p(\%)$	$m_{\text{ext}} (\mu\text{m}^{-1})$	g	$p(\%)$	$p(\%)$
	Dependence on k	stable	Dependence on k	Dependence on k	stable	Proportional to P_d	stable	stable	stable	stable

Note: m_{ext} : lighthextinction factor, g : anisotropy factor, n : refractive index (real part), p : light absorption probability, k : refractive index (imaginary part), λ : light wavelength, r : grain radius, P_d : packing density

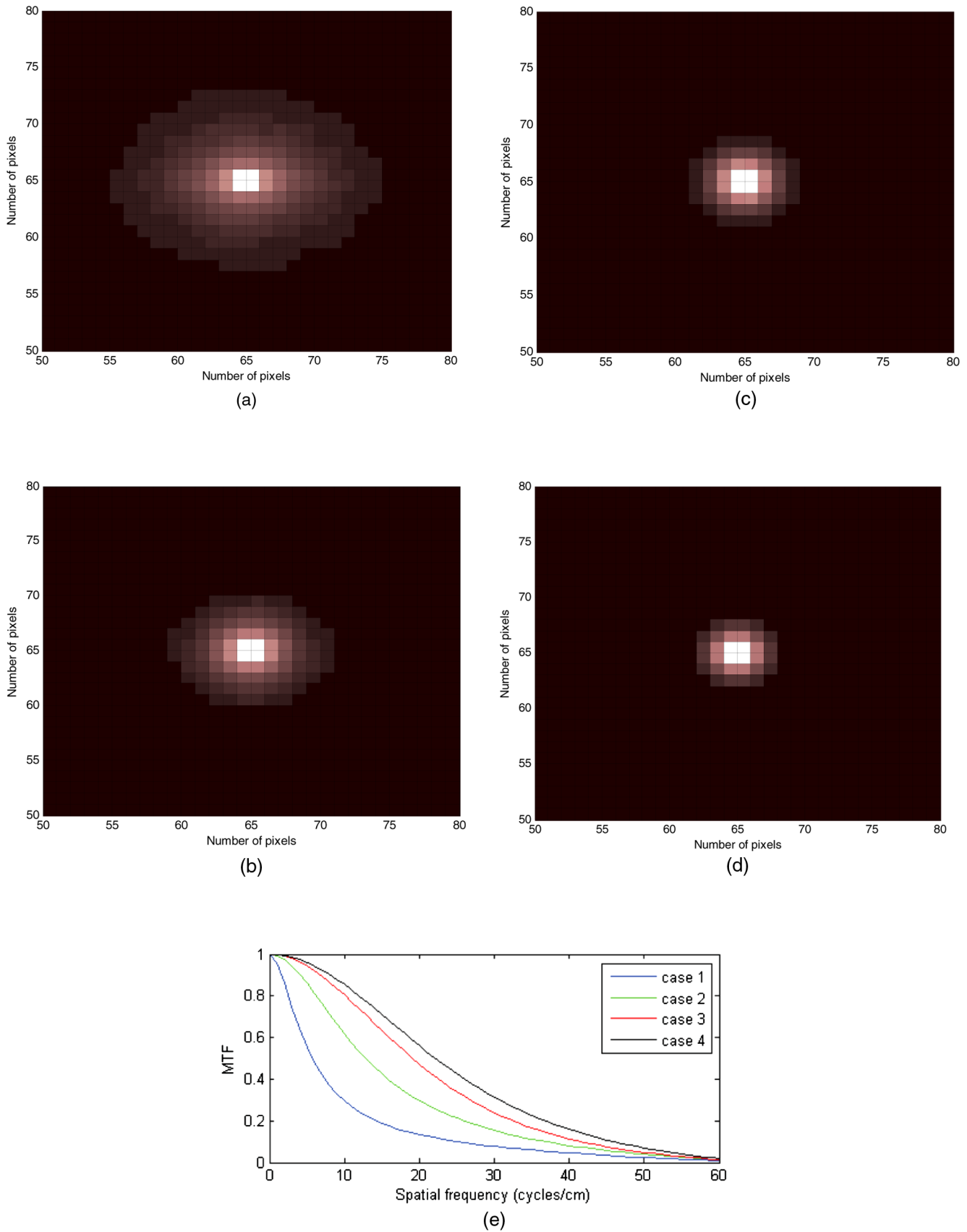


Fig. 3 The ground side PSF of the four nanophosphor categories: [(a) case 1, (b) case 2, (c) case 3, and (d) case 4] and the corresponding MTF (e) of all cases. signal modulation improvement (v) considering comparisons between cases (2), (3), (4) with case (1) Figures refer to a nanophosphor layer of common thickness (200 micrometers). The PSF is illustrated considering pixel size $78.125 \mu\text{m}$. The MTF percentage (%) signal modulation improvement is depicted as a function of spatial frequency (cycles/cm): Case (a)—blue, Case (b)—green, Case (c)—red and Case (d)—black.

4 Conclusion

Nanophosphors are a new class of advanced materials exhibiting unique structural and optical properties compared to those of their bulk materials. The present study aimed: (1) to analyze the optical transport within luminescent nanomaterials, (2) to examine nanophosphor-based materials of various properties, (3) to enhance research activities in the field of medical imaging detectors design and evaluation. Optimum optical parameters were predicted indicating the corresponding structural and optical properties of nanophosphors significantly promising in manufacture for further signal modulation improvement. Results showed that high optical diffusion performance of nanophosphors is accomplished with grains of high refractive index and size above 100 nm (grain radius).

Appendix A: Mie Scattering Optical Parameters

Mie theory provides a complete analytical solution of optical photon interactions with spherical phosphor grains.²⁰ Analysis of the Mie scattering algorithm requires three optical parameters: (a) the light extinction coefficient, m_{ext} and (b) the anisotropy scattering factor, g and (c) the light absorption probability p .

A.1 Evaluation of Light Extinction Coefficient m_{ext}

In the framework of Mie scattering theory light attenuation is expressed through the light extinction coefficient m_{ext} , which is expressed as follows:¹²

$$m_{\text{ext}} = V_d A Q_{\text{ext}}, \quad (1)$$

where V_d is the volume density of the phosphor material, A is the geometrical cross-section of the grain and Q_{ext} is the extinction efficiency factors. The volume density V_d of the phosphor screen as well as the geometrical cross-section of the grain A can be determined as follows:

$$V_d = \frac{P_d}{\frac{1}{6}\pi d^3} \quad \text{and} \quad A = \pi d^2/4, \quad (2)$$

where p_d is the packing density of the granular phosphor and d is the diameter of the phosphor grain. The corresponding extinction Q_{ext} is given by the following expressions:

$$Q_{\text{ext}} = \frac{2}{x^2} \sum_{n=1}^{\infty} (2n+1) \text{Re}(a_n + b_n), \quad (3)$$

where a_n and b_n are the so-called Mie coefficients, expressed as:²⁰

$$a_n = \frac{\psi_n'(mx)\psi_n(x) - m\psi_n(mx)\psi_n'(x)}{\psi_n'(mx)\zeta_n(x) - m\psi_n(mx)\zeta_n'(x)}, \quad (4)$$

$$b_n = \frac{m\psi_n'(mx)\psi_n(x) - \psi_n(mx)\psi_n'(x)}{m\psi_n'(mx)\zeta_n(x) - \psi_n(mx)\zeta_n'(x)},$$

where m is the relative complex refractive index and equal to the ratio $n_{\text{grain}}/n_{\text{medium}}$, where n_{grain} is the complex refractive index $[n(\omega) + i(k(\omega))]$ of the phosphor grains and n_{medium} is the refractive index of the of the medium. x is the size parameter of Mie

theory $x = \pi d n_{\text{medium}}/\lambda$, where λ is the wavelength of light and $\psi_n(x)$ and $\zeta_n(x)$ are the Riccati-Bessel functions. The calculation of Riccati-Bessel functions can be carried out by the following recurrences, taking into account their corresponding properties:

$$\begin{aligned} \psi_{n+1}(x) &= (2n+1)\psi_n(x)/x - \psi_{n-1}(x) \\ \zeta_{n+1}(x) &= (2n+1)\zeta_n(x)/x - \zeta_{n-1}(x) \\ \psi_n'(x) &= \psi_{n-1}(x) - n\psi_n(x)/x \\ \zeta_n'(x) &= \zeta_{n-1}(x) - n\zeta_n(x)/x \\ \psi_{-1}(x) &= \cos(x), \\ \psi_0(x) &= \sin(x) \\ \zeta_{-1}(x) &= \cos(x) - i \sin(x), \\ \zeta_0(x) &= \sin(x) + i \cos(x). \end{aligned} \quad (5)$$

The infinite summations in Eq. (5) for the extinction efficiency factors calculations converge after a certain number $N_{\text{max}} = x + cx^{1/3} + b$, where $c = 4$ and $b = 2$ depending on x . Usually the recursion formulas are used up to N_{max} th order.

A.2 Evaluation of Anisotropy Scattering Factor g

Light attenuation is described through absorption and scattering expressed by the corresponding coefficients m_{abs} , m_{sct} as given below:

$$m_{\text{abs}} = V_d A Q_{\text{abs}} \quad \text{and} \quad m_{\text{sct}} = V_d A Q_{\text{sct}}, \quad (6)$$

where Q_{abs} and Q_{sct} are the corresponding absorption and scattering efficiency factors, which are given below:¹²

$$Q_{\text{sct}} = \frac{2}{x^2} \sum_{n=1}^{\infty} (2n+1) (|a_n|^2 + |b_n|^2), \quad (7)$$

$$Q_{\text{abs}} = Q_{\text{ext}} - Q_{\text{sct}}.$$

At the site of light photon interaction, the type of interaction may be determined by the relative probabilities of light absorption and light scattering effects. The probability of light absorption p is defined as follows:

$$p = \frac{m_{\text{abs}}}{m_{\text{abs}} + m_{\text{sct}}}. \quad (8)$$

In case of light scattering, the new direction of light photon is also affected by the size of phosphor grains, the light wavelength and the refractive index of the phosphor. In the present study the new light photon direction was expressed through the so-called anisotropy factor g . In this case, the new polar angle of the light photon is obtained according to Henyey-Greenstein distribution and the anisotropy factor was calculated using the following equation:

$$g = \frac{\int_0^\pi 2\pi S_{11}(\theta) \cos \theta \sin \theta d\theta}{\int_0^\pi 2\pi S_{11}(\theta) \sin \theta d\theta}, \quad (9)$$

where $S_{11}(\theta)$ is the first element of the so-called Mueller matrix, which implies that light extinction is independent of the light polarization state. $S_{11}(\theta)$ is associated to the complex elements of scattering matrix $S_1(\theta)$ and $S_2(\theta)$ as follows.²¹

$$S_{11}(\theta) = \frac{1}{2}|S_1(\theta)|^2 + \frac{1}{2}|S_2(\theta)|^2, \quad (10)$$

where

$$S_1(\theta) = \sum_{n=1}^{\infty} \frac{2n+1}{n(n+1)} [a_n \pi_n(\cos \theta) + b_n \tau_n(\cos \theta)], \quad (11)$$

and

$$S_2(\theta) = \sum_{n=1}^{\infty} \frac{2n+1}{n(n+1)} [b_n \pi_n(\cos \theta) + a_n \tau_n(\cos \theta)]. \quad (12)$$

The angle-dependent functions π_n and τ_n were computed by upward recurrence from the following relations:

$$\pi_n = \frac{2n-1}{n-1} \cos \theta \pi_{n-1} - \frac{n}{n-1} \pi_{n-2}, \quad (13)$$

and

$$\tau_n = n \cos \theta \pi_n - (n+1) \pi_{n-1}, \quad (14)$$

beginning with $\pi_0 = 0$ and $\pi_1 = 1$.

Appendix B: Modeling Optical Diffusion

A light photon history was considered to start within the phosphor layer with the coordinates of the initial position (at the half of nanophosphor thickness, see Sec. 2.3) and the initial direction angles (polar and azimuthal) determined by an isotropic distribution. Setting different sequences of random numbers R_1 , R_2 , R_3 and R_4 , the polar angle θ and the azimuthal angle ϕ were sampled according to the following relations:

$$\begin{aligned} x_{o1} &= 2R_1 - 1, \\ y_{o1} &= 2R_2 - 1, \\ x_{o2} &= 2R_3 - 1, \quad \text{and} \\ y_{o2} &= 2R_4 - 1 \end{aligned} \quad (15)$$

$$\sin(\varphi) = (2x_{o1}y_{o1})/(x_{o1}^2 + y_{o1}^2), \quad (16)$$

$$\cos(\varphi) = (x_{o1}^2 - y_{o1}^2)/(x_{o1}^2 + y_{o1}^2), \quad (17)$$

$$\sin(\theta) = (2x_{o2}y_{o2})/(x_{o2}^2 + y_{o2}^2), \quad (18)$$

$$\cos(\theta) = (x_{o2}^2 - y_{o2}^2)/(x_{o2}^2 + y_{o2}^2). \quad (19)$$

Just after their creation, light photons are transmitted through the screen material towards the screen surfaces according to the following procedures:

1. Light photon attenuation: The light photon transport through the material was described in terms of the mean photon free path length fpl and the co-ordinates of the interaction site. The fpl was obtained as follows:

$$fpl = -\frac{1}{m_{\text{ext}}} \ln R_5, \quad (20)$$

where m_{ext} is the light extinction coefficient and R_5 is a random number uniformly distributed in the interval (0,

1]. The co-ordinates of the light photon interaction site were calculated from the free path length and the direction of the light photon, as it is given below:

$$\begin{pmatrix} x_{n+1} \\ y_{n+1} \\ z_{n+1} \end{pmatrix} = \begin{pmatrix} x_n \\ y_n \\ z_n \end{pmatrix} + fpl \begin{pmatrix} a \\ b \\ c \end{pmatrix}, \quad (21)$$

where $(x_{n+1}, y_{n+1}, z_{n+1})$, (x_n, y_n, z_n) are the coordinates of two successive interaction sites and (a, b, c) is a vector representing the direction cosines of the x-ray photon trajectory, given by $(a, b, c) = (\sin \theta \cos \phi, \sin \theta \sin \phi, \cos \theta)$. θ and ϕ are the polar and azimuthal angles, respectively, which were initially determined from the considered beam geometry.

2. Light photon interaction: At the site of light photon interaction, the type of interaction may be determined by the relative probabilities of light absorption and light scattering effects. The probability of light absorption p is calculated by using the light absorption and light scattering coefficients m_{abs} , m_{sct} , respectively. In case of light scattering, light photons continue attenuation (i.e., procedure 1) after the selection of the coordinates of the scattered light photon. The cosines of this new direction are transformed into a global (laboratory) coordinate system, as follows:

$$\begin{pmatrix} a' \\ b' \\ c' \end{pmatrix} = \begin{pmatrix} \cos \phi \cos \theta & -\sin \phi & \cos \phi \sin \theta \\ \sin \phi \cos \theta & \cos \theta & \sin \phi \sin \theta \\ -\sin \theta & 0 & \cos \theta \end{pmatrix} \begin{pmatrix} a \\ b \\ c \end{pmatrix}, \quad (22)$$

where $(a, b, c) = (\sin \theta \cos \phi, \sin \theta \sin \phi, \cos \theta)$ are the sampled direction cosines and θ , ϕ are the polar and azimuthal angles of the x-ray photon trajectory before scattering, i.e., a coordinate system with origin at the interaction point and the z-axis along the initial photon direction, and $(a', b', c') = (\sin \theta' \cos \phi', \sin \theta' \sin \phi', \cos \theta')$ are the direction cosines in the global coordinate system (laboratory frame).

3. Light scattering: The azimuthal angle ϕ of the scattered photon was sampled randomly in $[0, 2\pi)$. The polar angle θ was sampled from the Henyey-Greenstein, as given below:¹²

$$\cos \theta = \frac{1}{2g} \left[1 + g^2 - \left(\frac{1 - g^2}{1 - g + 2gR_6} \right)^2 \right] \quad (23)$$

when $g \neq 0$.

The free parameter g is the anisotropy factor, which implies isotropic distribution of light for $g = 0$ and sharply forward direction of light for $g = 1$. R_6 is a random number uniformly distributed in the interval (0, 1].

Appendix C: Modulation Transfer Function

The MTF metric is defined as the ratio of the modulation of the output signal over the modulation of an input signal of the same frequency, given by Refs. 1 and 11:

$$\text{MTF}(f) = \frac{|T(f)|}{T(0)}, \quad (24)$$

where the factor $T(f)$ is called the characteristic function of the system and $\text{MTF}(f)$ has by definition a value of unity at $f = 0$. To evaluate MTF, a two dimensional PSF is obtained by the optical photon distribution emitted by the x-ray converter, and, then, a fast Fourier transform (FFT) is employed to the one-dimensional line spread function LSF normalizing its value to unity at zero spatial frequency. The LSF describes the response of the system in one direction when details of the response in the orthogonal direction have been integrated out. Therefore, the system response along a line in the perpendicular direction is given by Ref. 31:

$$\text{LSF}(x) = \frac{\int_{-\infty}^{+\infty} \text{PSF}(x, y) dy}{\int_{-\infty}^{+\infty} \int_{-\infty}^{+\infty} \text{PSF}(x, y) dx dy}. \quad (25)$$

The MTF graph is used to obtain the relative image quality degradation in the spatial frequency domain and to evaluate the resolution of the screen. The MTF graph is used to obtain the relative image quality degradation at spatial frequencies. Assuming a square pixel geometry (having the size of d) to count light photons at the output of the layer, the theoretical MTF due to an aperture function can be expressed by the ‘‘sinc’’ function, as follows:

$$\text{MTF}_{\text{Pixel}}(f) = \frac{\sin(\pi df)}{\pi df}, \quad (26)$$

and then the MTF of the phosphor is given by the following relation:

$$\text{MTF}_{\text{Phosphor}}(f) = \frac{\text{MTF}_{\text{Overall}}(f)}{\text{MTF}_{\text{Pixel}}(f)}. \quad (27)$$

Appendix D: Strain Effects on Optical Parameters

In classical electrodynamic theory, the dielectric function of material is independent of size.²⁹ However, a large number of studies have clearly demonstrated that as nanocluster size decreases there is a dramatic increase in the Plasmon resonance bandwidth which may be accompanied by shifts in the resonance position. To account for these findings, the basic Mie theory has been extended to include the fundamental assumption that the dielectric function of nanoparticles is size dependent, thus explaining the dependence of resonance bandwidth on particle radius.^{42–44} To this aim the dielectric function can be modified including the damping effects affecting also the optical attenuation properties of the material expressed by the complex refractive index. The complex refractive index can be expressed as a function of the dielectric function according to relation below:

$$[n(\omega) + ik(\omega)]^2 = \epsilon_{\text{bulk}}(\omega). \quad (28)$$

The bulk dielectric function is often expressed as a combination of two terms, a Drude-Sommerfeld model for the free or

conduction electrons, and a core term representing the bound electrons as given below:

$$\epsilon_{\text{bulk}}(\omega) = \epsilon_{\text{core}}(\omega) + \epsilon_{\text{free}}(\omega) - 1. \quad (29)$$

Taking into account the free electron $\epsilon_{\text{free}}(\omega)$ term for semiconductors, Eq. (36) can be written as follows:³⁵

$$\epsilon_{\text{free}}(\omega) = \epsilon_{\text{core}}(\omega) - \frac{\omega_p^2}{\omega^2 + i\gamma\omega}, \quad (30)$$

where γ is the carrier damping constant and ω_p is the plasma frequency of the semiconductor as given below:³⁵

$$\omega_p^2 = \frac{Ne^2}{\epsilon_0 m_{\text{eff}} a^3}, \quad (31)$$

where e is the electric charge, N/a^3 is the carrier density m_{eff} is the effective mass of the electron, ϵ_0 is the free-space permittivity (8.854×10^{-12} F/m) and a is the deformed or strained lattice constant and can be expressed as follows:

$$a = a_0 + [\text{strain}(\%) \times a_0], \quad (32)$$

where a_0 is the lattice constant of the semiconductor and strain (%) is a factor that denotes the % strain of the lattice constant. Furthermore any strain-induced strain in lattice constant also impacts the Fermi velocity which in turn affects the carrier damping constant γ as follows:³⁵

$$\gamma = \gamma_0 + \left(A \frac{V_F}{L_{\text{eff}}} \right), \quad (33)$$

where A is a dimensionless parameter, L_{eff} is the reduced effective mean free path and V_F is given by the following analytic expression:

$$V_F = \sqrt{\frac{2E_F}{m}}, \quad (34)$$

where E_F is the Fermi energy expressed by the following relation:

$$E_F = \frac{h^2}{2m} \left(\frac{3}{8\pi} \right)^{2/3} N^{2/3}, \quad (35)$$

where h is Planck’s constant, m is the electron mass. Finally, imposed mechanical strain also affects the dielectric function of the ionic core, or bound electrons according to the following formula:

$$\epsilon_{\text{core}}(\omega) \rightarrow \frac{\epsilon_{\text{core}}(\omega) + 2 + 2\nu[\epsilon_{\text{core}}(\omega) - 1]}{\epsilon_{\text{core}}(\omega) + 2 - \nu[\epsilon_{\text{core}}(\omega) - 1]}, \quad (36)$$

where ν captures the strain-induced change in lattice constant $\nu = (\frac{a_0}{a})^3$. As shown in Fig. 4, employing the above formulas on ZnO single crystal, the refractive index decreases approximately 15.25% (real part) and 13.90% (imaginary part), respectively for a given light wavelength, considering the following parameters:^{45,46} (a) $N/a^3 = 1/10^{18}$ cm³, (b) $a_0 = 4.566\text{\AA}$, (c) $\epsilon_{\text{core}} = 3.705$, (d) $\bar{m}_{\text{eff}} = 0.7 m_{\text{electron}}$.

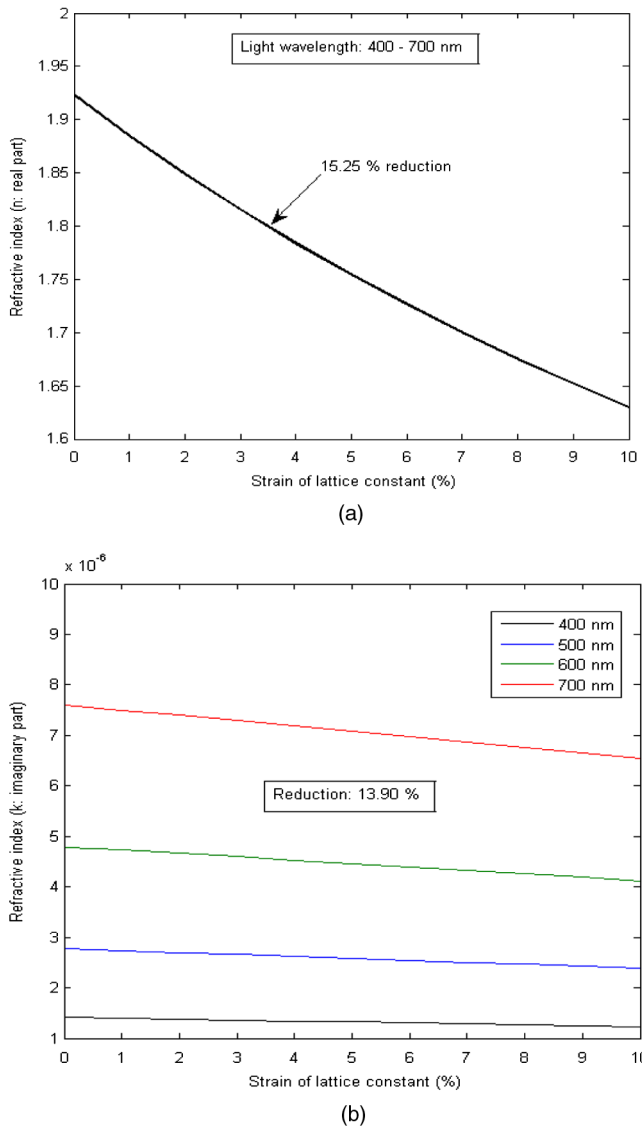


Fig. 4 The variation of refractive index: (a) real part n and (b) imaginary part k , as a function of the strain of lattice constant (%) of ZnO single crystal. The refractive index decreases approximately 15.25% (real part) and 13.90% (imaginary part), respectively for a given light wavelength, considering the following parameters: (a) $N/a^3 = 1/10^{18} \text{ cm}^{-3}$, (b) $a_0 = 4.566 \text{ \AA}$, (c) $\epsilon_\infty = 3.705$, (d) $\tilde{m}_{\text{eff}} = 0.7m_{\text{electron}}$.

References

- J. T. Dobbins III, "Image quality metrics for digital systems," in *Handbook of Medical Imaging, I. Physics and Psychophysics*, J. Beutel, H. L. Kundel, and R. L. Van Metter, Eds., pp. 161–229, SPIE, Bellingham, WA (2000).
- C. W. E. van Eijk, "Inorganic scintillators in medical imaging," *Phys Med. Biol.* **47**(8), R85–R106 (2002).
- H. Chander, "Development of nanophosphors," *Mater. Sci. Eng.* **49**(5), R113–R155 (2005).
- G. Blasse, "Classical phosphors: a Pandora's box," *J. Lumin.* **72–74**, 129–134 (1997).
- J. L. West and N. J. Halas, "Engineered nanomaterials for biophotonics applications: improving sensing, imaging, and therapeutics," *Annu. Rev. Biomed. Eng.* **5**, 285–292 (2003).
- D. K. Chatterjee, A. J. Rufaihah, and Y. Zhang, "Upconversion fluorescence imaging of cells and small animals using lanthanide doped nanocrystals," *Biomaterials* **29**(7), 937–943 (2008).

- E. B. Voura et al., "Tracking metastatic tumor cell extravasation with quantum dot nanocrystals and fluorescence emission-scanning microscopy," *Nat. Med.* **10**(9), 993–998 (2004).
- R. N. Bhargava and D. Gallagher, "Optical properties of manganese-doped nanocrystals of ZnS," *Phys. Rev. Lett.* **72**(3), 416–419 (1994).
- R. N. Bhargava, "Composite nanophosphor screen for detecting radiation," U.S. Patent No. 5952665 (1999).
- M. Mappararu, "New nanophosphor scintillators for solid-state digital dental Imager," *Dentomaxillofac. Rad.* **35**(6), 475–476 (2006).
- I. A. Cunningham, "Applied linear-systems theory," in *Handbook of Medical Imaging, I. Physics and Psychophysics*, J. Beutel, H. L. Kundel, and R. L. Van Metter, Eds., pp. 82–157, SPIE, Bellingham, WA (2000).
- P. Liaparinos et al., "Modeling granular phosphor screens by Monte Carlo methods," *Med. Phys.* **33**(12), 4502–4514 (2006).
- M. J. Weber, "Inorganic scintillators: today and tomorrow," *J. Lumin.* **100**(1–4), 35–45 (2002).
- G. Loewenstein, "The psychology of curiosity: a review and reinterpretation," *Psychol. Bull.* **116**, 75–98 (1994).
- A. Kienle, "Anisotropic light diffusion: an oxymoron?," *Phys. Rev. Lett.* **98**(21), 218104 (2007).
- D. W. O. Rogers, "Fifty years of Monte Carlo simulations for medical physics," *Phys. Med. Biol.* **51**(13), R287–R301 (2006).
- P. Liaparinos and I. Kandarakis, "The Monte Carlo evaluation of noise and resolution properties of granular phosphor screens," *Phys. Med. Biol.* **54**(4), 859–874 (2009).
- A. Badano and J. Sempau, "MANTIS: combined x-ray, electron and optical Monte Carlo simulations of indirect radiation imaging systems," *Phys. Med. Biol.* **51**(6), 1545–1561 (2006).
- P. R. Granfors and D. Albagli, "Scintillator-based flat-panel x-ray imaging detectors," *J. Soc. Inf. Display* **17**(6), 535–542 (2009).
- H. C. Van de Hulst, *Light Scattering by Small Particles*, Wiley, New York (1957).
- C. F. Bohren and D. R. Huffman, *Absorption and Scattering of Light by Small Particles*, Wiley, New York (1983).
- F. Allhoff, P. Lin, and D. Moore, *What is Nanotechnology and Why Does It Matter?: From Science to Ethics*, pp. 3–5, John Wiley and Sons, West Sussex, United Kingdom (2010).
- G. Blasse, "The luminescent efficiency of scintillators for several applications: state-of-the-art," *J. Lumin.* **60–61**, 930–935 (1994).
- L. E. Brus, "Electron-electron and electron-hole interactions in small semiconductor crystallites: the size dependence of the lowest excited electronic state," *J. Chem. Phys.* **80**(9), 4403–4409 (1984).
- A. G. Webb, "X-ray imaging and computed tomography," in *Introduction to Biomedical Imaging*, S. V. Kartalopoulos, Ed., pp. 253–274, John Wiley & Sons, Hoboken, New Jersey (2003).
- R. M. Nishikawa, "The fundamentals of MTF, Wiener Spectra, and DQE," in *Proc. 4th Annual meeting of the American Association of Physicists in Medicine*, San Antonio, Texas (1998).
- H. S. Yoo, S. W. Kim, and D. Y. Jeon, "Synthesis of phosphor photonic crystals by self-assembly of $\text{SiO}_2/\text{Y}_2\text{O}_3:\text{Tb}^{3+}$ core/shell particles and its photoluminescence properties," *J. Electrochem. Soc.* **157**(10), J358–J363 (2010).
- E. A. McKigney et al., "Nanocomposite scintillators for radiation detection and nuclear spectroscopy," *Nucl. Instrum. Methods. Phys. Res. A* **490**(1), 614–629 (2002).
- F. Wooten, *Optical Properties of Solids*, Academic Press, London, Toronto, Sydney, San Francisco (1972).
- S. M. Gruner, M. W. Tate, and E. F. Eikenberry, "Charge-coupled device area x-ray detectors," *Rev. Sci. Instrum.* **73**, 2816–2842 (2002).
- P. Liaparinos and I. Kandarakis, "The imaging performance of compact $\text{Lu}_2\text{O}_3:\text{Eu}$ phosphor screens: Monte Carlo simulation for applications in mammography," *Med. Phys.* **36**(6), 1985–1997 (2009).
- G. Blasse and B. C. Grabmaier, *Luminescent Materials*, Springer, Berlin (1994).
- P. Liaparinos and I. Kandarakis, "Overestimations in zero frequency DQE of x-ray imaging converters assessed by Monte Carlo techniques based on the study of energy impartation events," *Med. Phys.* **38**(7), 4440–4450 (2011).
- A. Rowlands and J. Yorkston, "Flat panel detectors for digital radiography," in *Handbook of Medical Imaging, Vol. 1: Physics and Psychophysics*, J. Beutel, H. L. Kundel, and R. L. Van Metter, Eds., pp. 223–328, SPIE, Bellingham, WA (2000).

35. X-H. Qian and H. S. Park, "The influence of mechanical strain on the optical properties of spherical gold nanoparticles," *J. Mech. Phys. Solids* **58**(3), 330–345 (2010).
36. E. Zych, J. Trojan-Piegza, and L. K. Kepinski, "Homogeneously precipitated $\text{Lu}_2\text{O}_3:\text{Eu}$ nanocrystalline phosphor for X-ray detection," *Sensor. Actuat. B-Chem.* **109**(1), 112–118 (2005).
37. D. Casanova et al., "Single europium-doped nanoparticles measure temporal pattern of reactive oxygen species production inside cells," *Nat. Nanotechnol.* **4**(9), 581–585 (2009).
38. G. M. Pavey, D. L. Copolov, and B. Dean, "High-resolution phosphor imaging: validation for use with human brain tissue sections to determine the affinity and density of radioligand binding," *J. Neurosci. Meth.* **116**(2), 157–163 (2002).
39. H. Menkara et al., "Development of nanophosphors for light emitting diodes," *Opt. Express* **19**, A972–A981 (2011).
40. J. F. Arregui, Ed., *Sensors Based on Nanostructured Materials*, Springer, New York (2008).
41. R. Xu, *Particle Characterization: Light Scattering Methods*, Kluwer Academic Publishers, New York, Boston, Dordrecht, London, Moscow (2002).
42. B. D. Milbrath et al., "Radiation detector materials: an overview," *J. Mater. Res.* **23**(10), 2561–2581 (2008).
43. C. N. R. Rao and A. K. Cheetham, "Science and technology of nanomaterials: current status and future prospects," *J. Mater. Chem.* **11**(12), 2887–2894 (2001).
44. P. Moriarty, "Nanostructured materials," *Rep. Prog. Phys.* **64**(3), 297–381 (2001).
45. M. Inoue, "Cathodoluminescence efficiency of binary compound phosphors," *J. Appl. Phys.* **55**(6), 1558–1565 (1984).
46. J. Han et al., "Optical and dielectric properties of ZnO tetrapod structures at terahertz frequencies," *Appl. Phys. Lett.* **89**(3), 031107 (2006).